Journal of the Korean Nuclear Society
Volume 36, Number 5, pp.375~387, October, 2004

Transient Multicomponent Mixture Analysis Based On an ICE Numerical Technique for the Simulation of an Air Ingress Accident in an HTGR

Hong Sik Lim
Korea Atomic Energy Research Institute
150 Deokjin-dong, Yuseong-gu, Daejon, Korea, 305-353
hslim@kaeri.re.kr

Hee Cheon NO
Korea Advanced Institute of Science and Technology
373-1 Guseong-dong, Yuseong-gu, Deajon, Korea 305-701

(Received September 1, 2003)

Abstract

This paper presents a transient multicomponent mixture analysis tool developed to analyze the molecular diffusion, natural convection, and chemical reactions related to air ingress phenomena that occur during a primary-pipe rupture of a high temperature gas-cooled reactor (HTGR). The present analysis tool solves the one-dimensional basic equations for continuity, momentum, energy of the gas mixture, and the mass of each gas species. In order to obtain numerically stable and fast computations, the implicit continuous Eulerian scheme is adopted to solve the governing equations in a strongly coupled manner. Two types of benchmark calculations were performed with the data of prerious Japanese inverse U-tube experiments. The analysis program, based on the ICE technique, runs about 36 times faster than the FLUENT6 for the simulation of the two experiments. The calculation results are within a 10% deviation from the experimental data regarding the concentrations of the gas species and the onset times of natural convection.

Key Words : HTGR, air ingress, molecular diffusion, natural convection, graphite oxidation

1. Introduction

High temperature gas-cooled reactors (HTGR) are drawing new attention in the nuclear energy field. The high temperature outputs of these reactors, as well as their outstanding passive and safe performances, establish the potential of HTGR to be environmentally-friendly electricity producers.

In accordance with safety requirements and with postulated accident scenarios, the HTGR design is

required to satisfy the fuel failure criterion (~1600 ℃). One of the postulated design basis accidents is a guillotine-type break of the main pipes connecting to the reactor vessel, as shown in Fig.1.

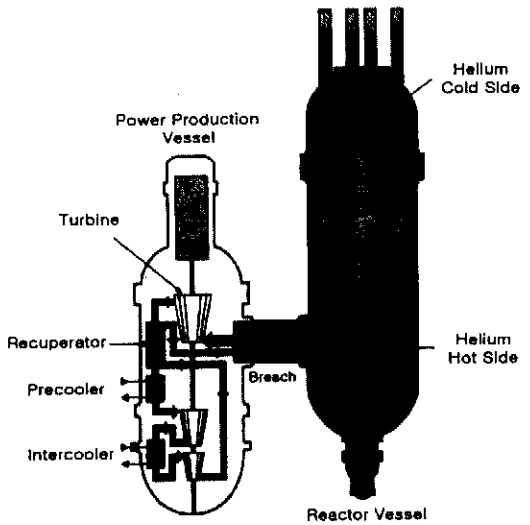

Fig. 1. Schematic Diagram of an HTGR

When this type of break occurs, helium in the reactor vessel is rapidly discharged into the reactor cavity and causes the reactor core to experience fuel heat-up, due to the mismatch between the decay heat and the heat removal through the reactor cavity coolers. At that time, the fuel temperature reaches the first peak. Subsequently, the fuel temperature begins to decrease slowly, because of continuous heat removal by passive cooling mechanisms.

After the break, the flow passage in the reactor vessel is simplified by an inverse U-shaped system. A hot leg consists of an inner passage of a coaxial duct, a high-temperature outlet mixing plenum, and a reactor core. A cold leg consists of an annular passage of the coaxial duct, a bottom space, an annular passage between the reactor pressure vessel and the inner vessel, and a top space. When the postulated guillotine break of the coaxial pipe occurs, the helium gas is discharged into the reactor cavity and, within a few minutes, the gas pressure is balanced between the inside of the reactor vessel and the reactor cavity. After the helium depressurization, air in the reactor cavity enters the reactor vessel through the breach, due to molecular diffusion and a weak natural convection induced by the non-uniform temperature distribution. During this diffusion-dominant stage, the air transport rate is very low; therefore, this process continues for a very long time. As air ingresses into the reactor core, the density of the gas mixture in the rector core gradually increases and therefore overcomes the gravitational force. Eventually, global natural convection throughout the inverse U-shaped system takes place and the convection-dominant stage begins. Oxygen in the air transported into the reactor vessel chemically reacts with the graphite components, producing carbon monoxide (CO) and carbon dioxide (CO_2) in addition to exothermic heat. Since the graphite oxidation is very active during the convection-dominant stage, due to high rate of air inflow, the graphite fuel temperature rapidly increases and the graphite components are rapidly gasified.

As a result, several days following the break, a second fuel temperature peak may take place due to exothermic heat generated by the graphite oxidation accompanied by air ingress though the breach. Therefore, during an air ingress accident, it is essential to ensure that the temperature of the graphite fuel does not exceed the safety limit maintaining the integrity of reactor's internal structures.

This paper is concerned with the development of an analysis tool to investigate the phenomena related to an air ingress accident and with the benchmark calculations obtained with this analysis tool, as applied to previous experiments in Japan.

The following key mechanisms during the air ingress accident are considered in the numerical model and are discussed in the benchmark calculations: the molecular diffusion in a multicomponent mixture, the production/depletion of gas species and heat generation due to chemical reactions, and the global natural circulation.

2. Governing Equations and Numerical Method

2.1. Governing Equations and Physical Models

The governing equations consist of the basic equations for continuity, momentum conservation, energy conservation of the gas mixture, and the mass conservation of each species. Each species equation contains the source terms to consider molecular diffusion in a multicomponent mixture, and homogeneous and heterogeneous chemical reactions. The equation of overall continuity is obtained by summing the conservation equations of all the gas species. The energy equation for the gas mixture includes the wall-to-fluid energy transfer, the thermal conduction, the inter-diffusion term for energy transfer due to molecular diffusion, and the heat generation from the chemical reactions. Five gas species (He, N_2, O_2, CO, and CO_2) are considered in the present analytical model, and it is assumed that each gas species and the gas mixture follow the equation of state for an ideal gas.

The equation of continuity for the gas mixture:

$$\frac{\partial \rho}{\partial t}+\frac{1}{A}\frac{\partial}{\partial z}(\rho VA)=\sum_s R_s \qquad (1)$$

The equation of momentum conservation:

$$\frac{\partial}{\partial t}(\rho V)+\frac{1}{A}\frac{\partial}{\partial z}(\rho V^2 A)=-\frac{\partial P}{\partial z}-\rho f V|V|-\rho g \qquad (2)$$

The equation of sensible energy conservation:

$$\frac{\partial}{\partial t}(\rho H)+\frac{1}{A}\frac{\partial}{\partial z}(\rho HVA)=\frac{1}{A}\frac{\partial}{\partial z}\left(\lambda A\frac{\partial T}{\partial z}\right)-\frac{1}{A}\frac{\partial}{\partial z}\left(A\sum_{s=1}^{m}H_s J_s\right)-\sum_s \Delta h_{f,s}^{o} R_s+h(T_w-T) \qquad (3)$$

The conservation equation of each species, s (s = N_2, O_2, CO, CO_2):

$$\frac{\partial}{\partial t}(\rho Y_s)+\frac{1}{A}\frac{\partial}{\partial z}(\rho Y_s VA)=-\frac{1}{A}\frac{\partial}{\partial z}(AJ_s)+R_s \qquad (4)$$

$(s=1 \text{ to } m-1)$ and for He, $Y_m=1-\sum_{s=1}^{m-1}Y_s$

The equation of state:

$$\rho=\frac{PW}{RT} \quad where\ W=\left(\sum_{s=1}^{m}Y_s/W_s\right)^{-1} \qquad (5)$$

The ordinary diffusion flux (Js) is given in two forms, [1] the full multicomponent diffusion by HCB and [2] the effective diffusion by the assumption that a dilute species, s, diffuses through a homogeneous mixture:

$$J_s=\rho\frac{W_s}{W^2}\sum_{k=1,k\neq s}^{m}\left[D_{sk}\nabla(Y_k W)\right] \qquad (6)$$

$$J_s=-\rho D_{s,mix}\nabla Y_s \quad where\ D_{s,mix}=\left(\sum_{k=1,k\neq s}^{m}X_k/D_{sk}\right)^{-1} \quad (m\geq 3) \qquad (7)$$

Although the full multicomponent diffusion form, represented by Eq. (6), predicts the accurate diffusion behaviors of gas species in a multicomponent mixture, the effective diffusion form, represented by Eq. (7), is generally used in numerical calculations, because of its computational efficeiency as well as its accuracy close to that of the full multiccomponent diffusion form. The friction factor and the heat transfer coefficient corresponding to the fully developed laminar flow are used, and the wall temperature is assumed to be kept constant in benchmark calculations. For each species and the gas mixture, physical properties, such as molar weight,

viscosity, thermal conductivity, and sensible enthalpy, are obtained from Refs. 2 and 3.

The most important chemical reactions between oxygen and graphite are the heterogeneous reactions

$$C + O_2 \rightarrow CO_2 + 3.935 \times 10^5 \text{ (J/mole)}$$
$$C + (1/2)O_2 \rightarrow CO + 1.105 \times 10^5 \text{ (J/mole)}$$
$$C + CO_2 \rightarrow 2CO - 1.725 \times 10^5 \text{ (J/mole)}$$

and the homogeneous reaction

$$CO + (1/2)O_2 \rightarrow CO_2 + 2.830 \times 10^5 \text{(J/mole)}.$$

For the CO combustion, the reaction rate is taken from Ref. 4 and is represented by

$$-\frac{dC_{CO}}{dt} = K_0 C_{CO} C_{O_2}^{1/2} C_{H_2O}^{1/2} \exp\left(-E_0 / \bar{R}T\right) \quad (8)$$

where $K_0 = 1.3\times10^{14}\ ml/mole\text{-}sec$ and $E_0 = 30\ kcal/mole$.

A reaction rate is expressed as,

$$r_{CO\text{-}O_2} = 1.3\times10^8 \exp\left(-15155.2/T\right),$$

and from Eq. (8), the dissipation/generation rates for each species are expressed as

$$R_{CO}^{\ hom} = -r_{CO\text{-}O_2}\rho\left(\frac{\rho^2}{WW_{O_2}}\right)^{0.5} Y_{CO}Y_{O_2}^{0.5}X_{H_2O}^{0.5} \quad (9a)$$

$$R_{O_2}^{\ hom} = 0.5\left(R_{CO}^{\ hom}\right)\frac{W_{O_2}}{W_{CO}} \quad (9b)$$

$$R_{CO_2}^{\ hom} = -\left(R_{CO}^{\ hom}\right)\frac{W_{CO_2}}{W_{CO}} \quad (9c)$$

For the graphite oxidation, the general chemical equation is expressed as.

$$C + zO_2 \rightarrow xCO + yCO_2. \quad (10)$$

A reaction rate is expressed as

$$r_{C\text{-}O_2} = K_0 \exp\left(-E_0 / \bar{R}T\right) P_{O_2}^{\ n}$$

where K_0 is the reaction constant, E_0 is the activation energy, and P_{O_2} is the oxygen partial pressure.

Several experiments [5, 6, 7, 8] were conducted for IG-110 nuclear-grade graphite and a few correlations [6, 9] have been discussed in the related literatures; however, discrepancies between the experimental data and correlations have been remarkable, as shown in Fig. 2. We produced an empirical correlation based on Fuller and Okoh's data [8]:

$$r_{C\text{-}O_2} = K_0 \exp\left(-188000/\bar{R}T\right)\left(P_{O_2}^{\ w}\right)^n \quad \left[kg/m^2\text{-}s\right]$$

where $K_0 = f(n)$ and the order of the reaction (n = 0.5~1) is supplied by the user.

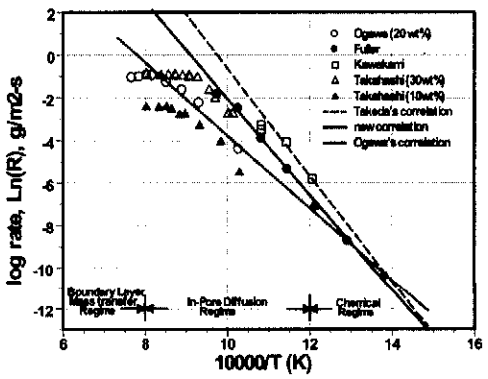

Fig. 2. Oxidation Data and Correlations for IG-110

A production ratio of CO and CO_2 ($x/y=fco/co_2$) for Eq. (10) is correlated as follows:

$$f_{co/co_2} = K_1 \exp\left(-E_1 / \bar{R}T\right)$$

where $K_1 = 1995$ and $E_1 = 59860$ [10].

Therefore, the mole number for the dissipation term of O_2 and the generation terms of CO and

CO_2 can be obtained from the following relations, respectively:

$$z=\frac{f_{CO/CO_2}+2}{2f_{CO/CO_2}+2},\ y=\frac{1}{f_{CO/CO_2}+1},\ x=\frac{f_{CO/CO_2}}{f_{CO/CO_2}+1}$$

The dissipation/generation rates for each species are expressed as

$$R_{O_2}^{het}=-zr_{C-O_2}\frac{W_{O_2}}{W_C} \tag{11a}$$

$$R_{CO}^{het}=xr_{C-O_2}\frac{W_{CO}}{W_C}, \tag{11b}$$

$$R_{CO_2}^{het}=yr_{C-O_2}\frac{W_{CO_2}}{W_C} \tag{11c}$$

Equation (11a) through (11c) are solved simultaneously with the fluid-to-surface mass transfer relationship:

$$R_s^{het}=\rho k_s\left(Y_s^w-Y_s\right),\quad for\ s=O_2,\ CO,\ CO_2 \tag{12}$$

where the mass transfer coefficient (k_s) is obtained by means of heat-mass transfer analogy, $Sh=k_s(d/D_{s\text{-}mix})=3.66(Sc/Pr)^{1/3}$.

2.2. Numerical Method

The governing equations are discretized in a semi-implicit manner in a staggered mesh layout and then the dependent variables are linearized by the Newton Raphson method. As a matrix reduction technique, the Implicit Continuous Eulerian (ICE) scheme [11] is adopted for a fast computation. In a staggered spatial nodding, the mesh cell configuration is:

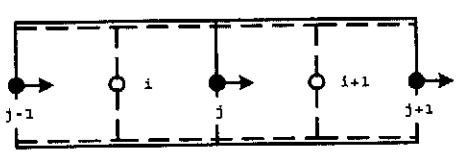

where i is the index of the scalar cell (solid box) and j is the index of the momentum cell (dashed box). An arrow indicates the flow direction from the upstream node to the downstream node.

In the ICE scheme, the non-conservative form of Eq. (2) is used, since the equation of momentum conservation should be expressed as a function of pressure only:

$$\frac{\partial V}{\partial t}+V\frac{\partial V}{\partial z}=-\frac{1}{\rho}\frac{\partial P}{\partial z}-g-fV|V| \tag{13}$$

Then, all of the conservation equations, Eqs. (1), (3), (4), and (13), are discretized as follows:

$$\frac{\rho_i^{n+1}-\rho_i^n}{\Delta t}+\frac{1}{Vol_i}\left(\dot{\rho}_j^{\,n}A_jV_j^{n+1}-\dot{\rho}_{j-1}^{\,n}A_{j-1}V_{j-1}^{n+1}\right)=\sum_s R_{s,i}^{n+1} \tag{14}$$

$$\frac{V_j^{n+1}-V_j^n}{\Delta t}+V_j^n\frac{\dot{V}_{i+1}^{\,n}-\dot{V}_i^n}{\Delta z_j}=-\frac{\left(P_{i+1}-P_i\right)^{n+1}}{\bar{\rho}_j^{\,n}\Delta z_j}-f_j^n\left(V^2\right)_j^{n+1}-g_j^n \tag{15}$$

$$\begin{aligned}&\frac{(\rho H)_i^{n+1}-(\rho H)_i^n}{\Delta t}+\frac{1}{Vol_i}\left(\dot{\rho}_j^{\,n}\dot{H}_j^{\,n}A_jV_j^{n+1}-\dot{\rho}_{j-1}^{\,n}\dot{H}_{j-1}^{\,n}A_{j-1}V_{j-1}^{\,n+1}\right)=\\&-\sum_s\Delta H_{f,s}^n R_{s,i}^{n+1}+\frac{1}{Vol_i}\left(\bar{\lambda}_j^{\,n}A_j\frac{T_{i+1}^{\,n}-T_i^n}{\Delta z_j}-\bar{\lambda}_{j-1}^{\,n}A_{j-1}\frac{T_i^n-T_{i-1}^{\,n}}{\Delta z_{j-1}}\right)\\&-\frac{1}{Vol_i}\left[A_j\sum_{s=1}^{ns}\left(\bar{H}_{s,j}^{\,n}J_{s,j}^{\,n}\right)-A_{j-1}\sum_{s=1}^{ns}\left(\bar{H}_{s,j-1}^{\,n}J_{s,j-1}^{\,n}\right)\right]+h_i^n\left(T_{wi}^n-T_i^{n+1}\right)\end{aligned} \tag{16}$$

$$\begin{aligned}&\frac{(\rho Y_s)_i^{n+1}-(\rho Y_s)_i^n}{\Delta t}+\frac{1}{Vol_i}\left(\dot{\rho}_j^{\,n}\dot{Y}_{s,j}^{\,n}A_jV_j^{n+1}-\dot{\rho}_{j-1}^{\,n}\dot{Y}_{s,j-1}^{\,n}A_{j-1}V_{j-1}^{\,n+1}\right)=\\&\frac{1}{Vol_i}\left(A_jJ_{s,j}^{\,n}-J_{s,j-1}^{\,n}A_{j-1}\right)+R_{s,i}^{n+1}\end{aligned} \tag{17}$$

where a bar (-) indicates average properties and a dot (·) indicates donor properties that depend on flow direction.

By the Newton method, pressure is linearized as $p^{n+1}\rightarrow p^k+\delta p$ and then inserted into Eq. (15), resulting in the following form:

$$V_j^{n+1}=V_j^k+Jacob_j\left(\delta P_i-\delta P_{i+1}\right) \tag{18}$$

where

$$Jacob_j = \frac{\Delta t}{\bar{\rho}_j^n \Delta z_j \left(1 + \Delta t 2 f_j^n |V_j^n|\right)}$$

$$V_j^k = \frac{V_j^n - \Delta t\left[V_j^n \frac{\dot{V}_{i+1}^n - \dot{V}_i^n}{\Delta z_j} - f_j^n V_j^n |V_j^n| + \frac{\left(P_{i+1}^k - P_i^k\right)}{\bar{\rho}_j^n \Delta z_j} + g_j^n\right]}{1 + \Delta t 2 f_j^n |V_j^n|}$$

Also, other dependent variables (ρ, Y_s, T, H) and source terms are linearized, as follows:

$$\begin{aligned} Y_s^{n+1} &\rightarrow Y_s^k + \delta Y_s, \quad T^{n+1} \rightarrow T^k + \delta T \\ \rho^{n+1} &\rightarrow \rho^k + \left(\frac{\partial \rho}{\partial P}\right)^k \delta P + \left(\frac{\partial \rho}{\partial T}\right)^k \delta T + \sum_s \left(\frac{\partial \rho}{\partial Y_s}\right)^k \delta Y_s \\ H^{n+1} &\rightarrow H^k + \left(\frac{\partial H}{\partial T}\right)^k \delta T + \sum_s \left(\frac{\partial H}{\partial Y_s}\right)^k \delta Y_s \\ R_s^{n+1} &\rightarrow R_s^k + \sum_s \left(\frac{\partial R_s}{\partial Y_s}\right)^k \delta Y_s \end{aligned} \tag{19}$$

By inserting V_j^{n+1} of Eq. (18) and the linearized variables of Eq. (19) into the discretized scalar equations, Eqs. (14), (16), and (17), and then combining the resulting equations into a linear algebraic form, a 6 ×6 square matrix is obtained:

$$\underline{\underline{B}}\,\delta \underline{X} = \underline{b} + \underline{c}\left(\delta P_{i+1} - \delta P_i\right) - \underline{d}\left(\delta P_i - \delta P_{i-1}\right)$$

where (20)

$$\underline{\underline{B}}\,\delta \underline{X} = \underline{b} + \underline{c}\left(\delta P_{i+1} - \delta P_i\right) - \underline{d}\left(\delta P_i - \delta P_{i-1}\right)$$

Multiplying Eq. (20) by the inverse matrix ($\underline{\underline{B}}^{-1}$), the solution vector is expressed as

$$\delta \underline{X} = \underline{\underline{B}}^{-1}\underline{b} + \underline{\underline{B}}^{-1}\underline{c}\left(\delta P_{i+1} - \delta P_i\right) - \underline{\underline{B}}^{-1}\underline{d}\left(\delta P_i - \delta P_{i-1}\right). \tag{21}$$

As a result, the first row in Eq. (21) becomes the N ×N pressure matrix and this pressure matrix is solved by a direct method using the Gauss elimination. The remaining rows in Eq. (21), the temperature and the mass fraction of each species, are expressed as a function of pressure only. As shown in Fig. 3, the above calculations are repeated until the convergence criterion,

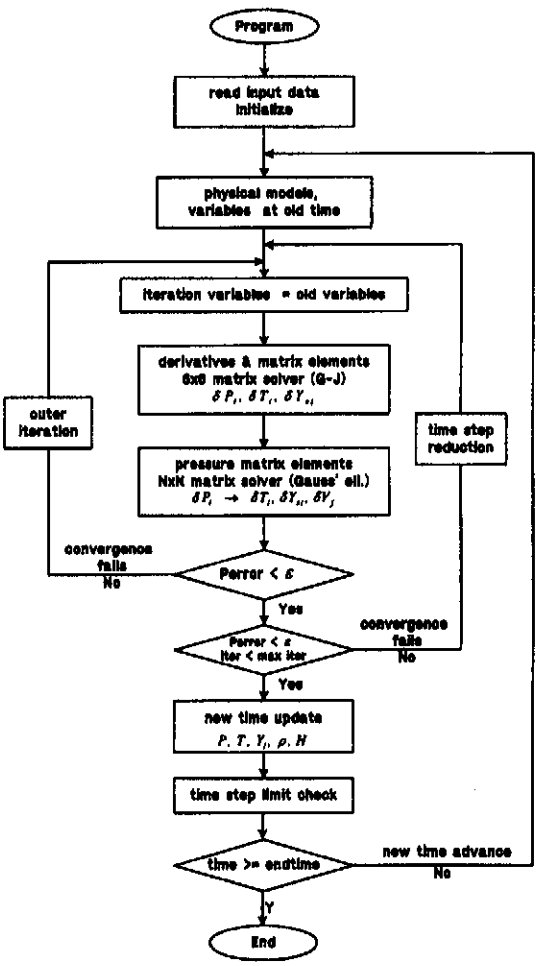

Fig. 3. Calculation Procedure of the Present Program

$\varepsilon = \max\left(\delta P_i / P_i^k\right)$, is satisfied. According to whether the convergence succeeds or fails, the time step is halved or doubled. However, the maximun time step size is restricted by the time step limit, $\Delta t_{max} \le \min\left(\Delta t_{convective}, \Delta t_{conducive}, \Delta t_{diffusive}\right)$, due to explicit treatment of the second-order terms.

3. Benchmark Calculations

3.1. Benchmarks for the Inverse U-tube Experiment in a Binary Mixture

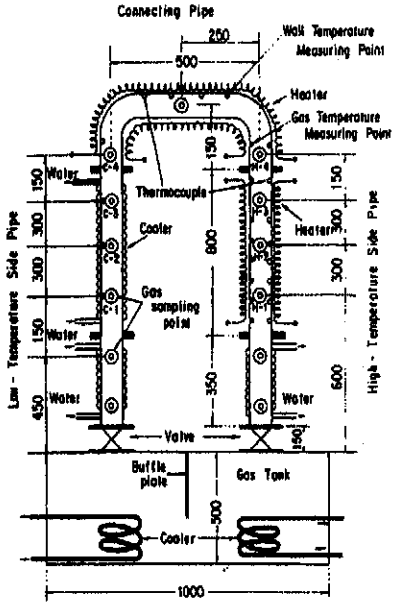

Fig. 4. Inverse U-tube Test Apparatus

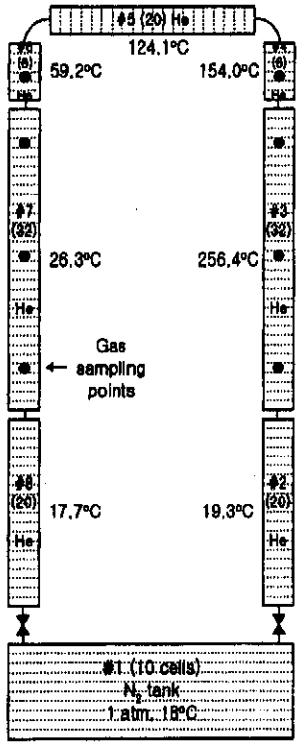

Fig. 5. Nodalization Diagram For the Inverse U-tube Test Apparatus

Figures 4 and 5 show the test apparatus [12] used to investigate the molecular diffusion behavior in the binary mixture and the nodalization diagram for the present model, respectively. The apparatus consists of an inverse U-shaped tube, with an inner diameter of 52.7 mm, and a gas tank. The ball valves between the reverse U-tube and the gas tank were closed and the tube was evacuated by means of a vacuum pump. The tube and the gas tank were filled with helium and nitrogen, respectively. Then, the high temperature side and the connecting pipes were heated to the elevated temperatures. When the temperatures of the gas and the pipe wall reached a steady state, the gas pressure in the reverse U-tube was equalized to the atmosphere pressure by opening a small release valve.

Two kinds of experiments were performed: the isothermal test and non-isothermal test. In the isothermal test, the inverse U-tube is kept at room temperature (18°C). In the non-isothermal test, the inverse U-tube has a non-uniform temperature distribution along the tube, as shown in Fig. 5. When the valves are opened simultaneously, N_2 gas in the bottom tank starts to diffuse into both sides of the inverse tube. The mole fraction of N_2 was obtained at eight sampling points (C-1

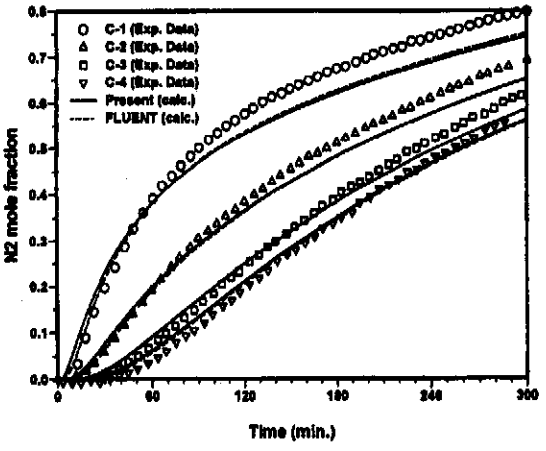

Fig. 6. Predicted Mole Fractions of N_2 (Isothermal Test)

through C-4 and H-1 through H-4), as shown in Fig. 4, by measuring the sound velocity of the gas mixture.

3.1.1. Isothermal Test

When the valves are opened, N_2 in the gas tank begins to move into the inverse tube filled with He by pure molecular diffusion. Because the mole fraction distribution of N_2 is the same between the hot and cold pipes, natural convection of the gas mixture does not occur. As shown in Fig. 6, the calculated results are within a 10% deviation from the experimental results, indicating a good agreement. The slight discrepancy with the experimental results seems to be caused by the entrance effect at the tube inlet, that is, a non-uniform concentration distribution.

3.1.2. Non-isothermal Test

The calculated results using a non-uniform temperature distribution are shown in Fig. 7. As the mole fraction of N_2 in the tube gradually increases, the buoyancy force induced by the distribution of the gas mixture density increases. Around 220 minutes after the valves are opened, the buoyancy force becomes large enough to initiate a global natural circulation throughout the inverse U-tube. The velocities caused by a very weak and global natural convection were calculated to be approximately $< 10^{-4}$ m/s in the early stage and 0.1 m/s (Re_d=500) in the later stage. The predicted results are within a 10% deviation from the experimental values measured at six sampling locations, indicating a good agreement. In particular, although the trends of the mole fractions of N_2 with respect to time are slightly different, the onset time of natural convection is nearly equal. As observed in the isothermal test, the slight discrepancy of the mole

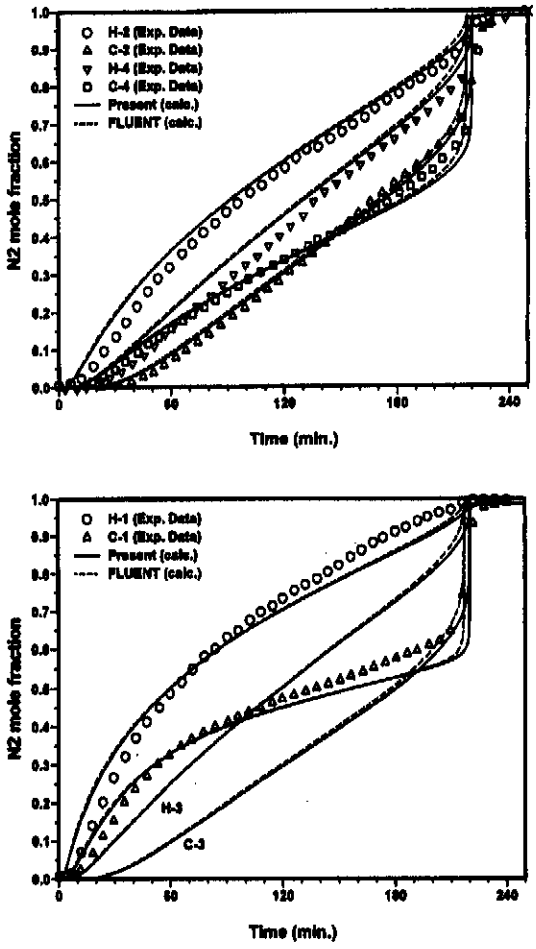

Fig. 7. Predicted Mole Fractions of N_2 (Non-Isothermal Test)

fractions of N_2 is attributed to the combination of the entrance effect at the tube inlet and the use of a rough temperature distribution along the tube.

3.1.3. Comparisons with FLUENT Simulations

Figures 6 and 7 also show the comparative results between the present calculations and the FLUENT simulations for both the isothermal and non-isothermal tests. The FLUENT6 [13] simulations are performed with the SIMPLE

Table 1. Computation Times and Time Steps for ICE and FLUENT

Test cases	Maximum time step		Computation time		Time step limit
	ICE	FLUENT	ICE	FLUENT	
Isothermal	0.5 sec	0.2 sec	32 min.	20 hrs	4.7 sec (diffusion)
Non-isothermal	0.5 sec	0.2 sec	36 min.	22 hrs	0.6-1.7 sec (conduction)

algorithm, using the 3-D mesh layout shown in Fig. 8. To reduce the computation time, the original circular geometry of the test apparatus was modified into a rectangular shape for generating coarse meshes by preserving the volumes of the bottom tank and the connecting pipe. The predicted trends are very similar in both the FLUENT and the present model. The remarkable point is the comparison of their computing times given in Table 1. Even though the number of mesh used in the FLUENT calculation is about twice that used in the present model, the FLUENT calculation is time consuming, taking nearly 40 times that of the present model. In addition, the maximum time step is lower than that of the present model.

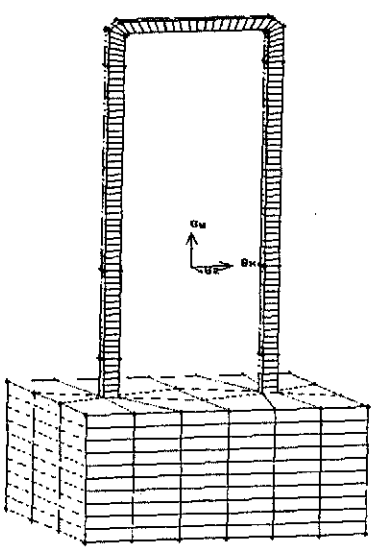

Fig. 8. FLUENT6 Mesh Layout for the Test Apparatus

3.2. Benchmark for the Inverse U-tube Experiment with a Graphite Tube

Figure 9 shows the experimental apparatus [9], consisting of a gas tank and an inverse U-shaped tube with a graphite (IG-110) tube inserted in the middle of the hot side, and Fig. 10 shows the nodalization diagram of the present model. The experimental procedure was identical to the one described in Section 3.1, except that the gas tank was filled with air instead of N_2. The mole fraction of each gas species and the density of the gas mixture were measured at four sampling points, as shown in Fig. 10, using a gas analyzer (Yokogawa: density-Vibro gas analyzer DG8, O_2-electrochemical analyzer 6234, CO and CO_2-

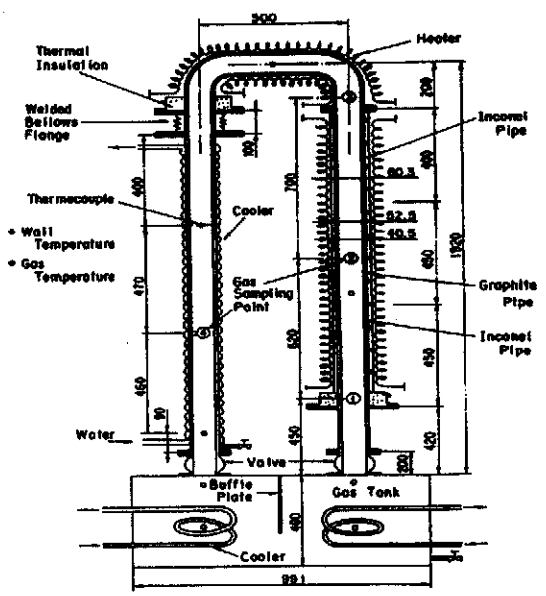

Fig. 9. Test Apparatus with a Graphite Tube

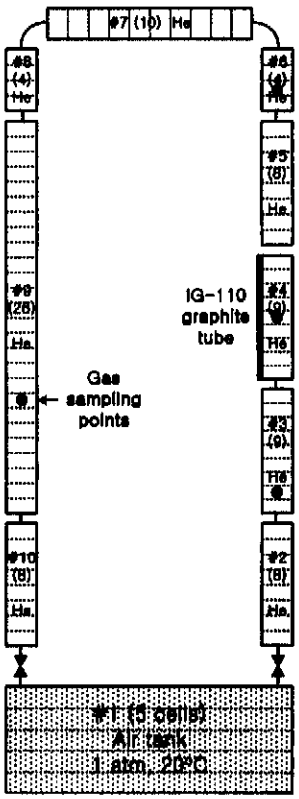

Fig. 10. Nodalization Diagram for the Test Apparatus with a Graphite Tube

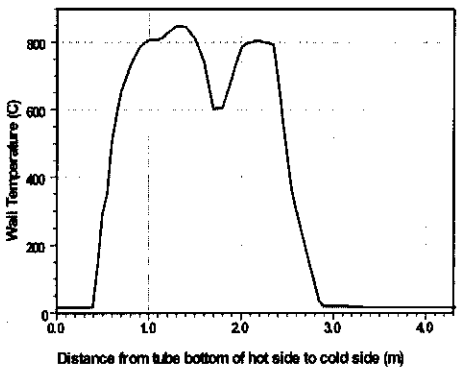

Fig. 11. Non-uniform Temperature Distribution Along the Inverse U-tube

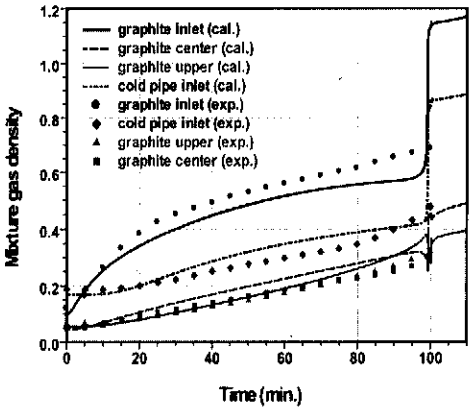

Fig. 12. Predicted Densities of the Gas Mixture

infrared rays analyzer IR21).

When the ball valves are opened, air enters into the vertical pipe by molecular diffusion and weak natural convection and then chemically reacts with the graphite. As the graphite is oxidized by a chemical reaction with oxygen, CO and CO_2 are produced and transported both upward and downward. A part of the CO produced dissipates by a homogeneous reaction with oxygen, and also a part of the CO_2 produced dissipates by a reverse reaction (Boudouard reaction) at a very high temperature. As time passes, the density of the gas mixture in the hot side increases gradually, eventually leading to a global natural convection. During the transient calculation, the non-uniform wall temperature distribution along the pipe shown in Fig. 11 is assumed to be kept constant. The CO_2 reverse reaction is not considered in the present calculation, because the graphite temperature is relatively low, being below 850°C.

Figures 12 through 16 show the predicted results of the densities of the gas mixture and the mole fractions of O_2, CO, and CO_2 at different sampling locations. As shown in Fig. 12, as N_2 and O_2 in the gas tank are transported into the tube, and as CO and CO_2 are produced by a chemical reaction with the graphite, the buoyancy force induced by the distribution of the gas mixture density gradually increases. Approximately 100 minutes after the valves are opened, the buoyancy force becomes large enough to initiate a global natural circulation throughout the inverse U-tube.

Figure 13 shows the velocities caused by a very weak and global natural convection calculated to be roughly $< 3\times10^{-4}$ m/s in the early stage and 0.2 m/s (Re_d=400) in the later stage. The range of the Rayleigh number, which is calculated based on the height of the inverse U-tube, is about $1\times10^{9}<Ra_H<5\times10^{10}$. As shown in Figs. 14 through 16, although the calculated mole fractions of O_2, CO, and CO_2 are slightly different from the measured mole fractions, the calculated onset time of natural convection agrees well with that of the experiment, because the density change of the gas mixture is less sensitive to the concentrations of each gas species.

In the present calculation, a value of 0.5 has been used for the order of the reaction (n) in the graphite oxidation correlation. Since the oxygen transported from the bottom tank is completely consumed within one-third the distance of the graphite tube from the inlet of the graphite tube, the produced CO and CO_2 are less sensitive to the order of the reaction (n) chosen. To obtain the prediction results for the CO mole fractions shown in Fig. 16, a small mole fraction of 0.5×10^{-6} was used for X_{H_2O} in the CO combustion correlation, because the effect of the moisture on CO

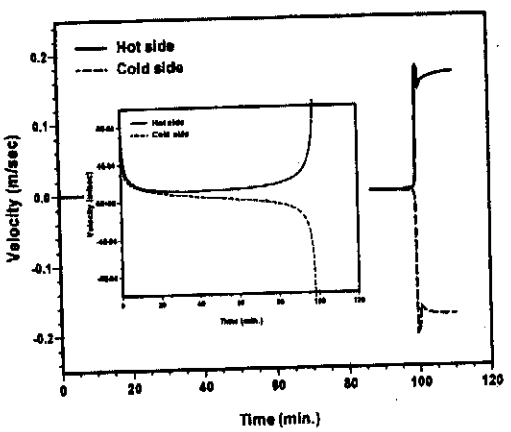

Fig. 13. Predicted Velocities at the Tube Inlet

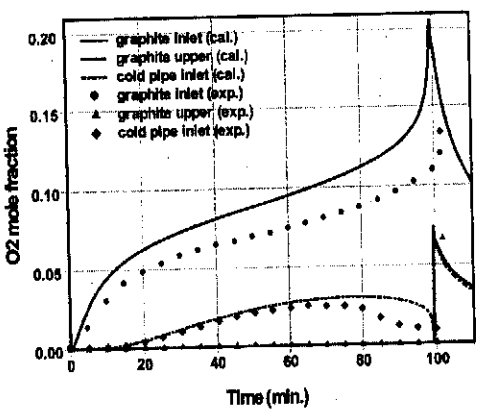

Fig. 15. Predicted Mole Fractions of CO_2

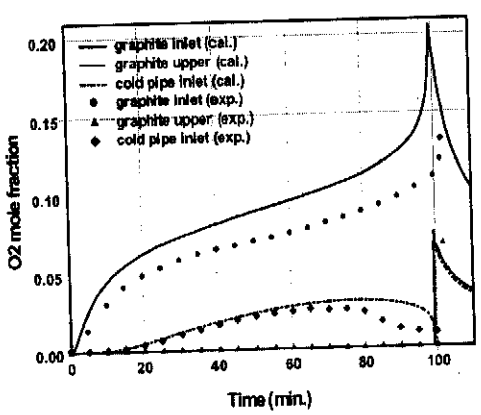

Fig. 14. Predicted Mole Fractions of CO_2

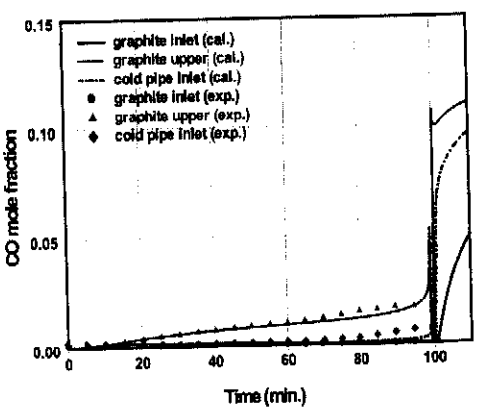

Fig. 16. Predicted Mole Fractions of CO

combustion is still uncertain.

4. Conclusions

In the benchmark calculations with the inverse U-tube experiments for both the isothermal and non-isothermal tests, the difference between the predicted results and the experimental data is within a 10% deviation regarding the concentrations of the species and the onset time of natural circulation. In addition, the calculation results of the present model are nearly identical to those of the FLUENT6 simulations, and the present program runs about 36 times faster than the FLUENT on a 900 MHz Pentium III PC.

In the benchmark calculation for the inverse U-tube experiment with a graphite specimen, the prediction results are within a 10% deviation from the experimental data, indicating a good agreement. Further investigations are necessary to justify the selected values for the order of the reaction for the graphite oxidation and for the initial mole fraction of moisture for the CO combustion, because there are few experimental works regarding the effects of these parameters.

Nomenclature

A = cross-sectional flow area (m^2)
C_s = concentration of species, s
d = hydraulic diameter (m)
D_{sk} = binary or multicomponent diffusion coefficient (m^2/s)
$D_{s\text{-}mix}$ = effective diffusion coefficient (m^2/s)
f = friction factor
f_{co/co_2} = production ratio of CO and CO_2 for graphite oxidation
g = gravitational constant
h = wall-to-fluid heat transfer coefficient (W/m^2-K)
$\triangle h_f^0$ = latent heat of formation for chemical reaction (J/kg)
H = sensible enthalpy of gas mixture (J/kg)
H_s = sensible enthalpy of species, s (s=He, N_2, O_2, CO, CO_2) (J/kg)
J_s = total diffusion flux with respect to mass average velocity (kg/m^2-s)
k_s = mass transfer coefficient of species, s (m/s)
m = total number of species
N = total number of scalar nodes or cells
P = total pressure (Pa)
P_{O_2} = oxygen partial pressure (Pa) in the bulk, and Po_2^w at the surface of the wall
$\bar{R}$ = universal gas constant
R_s = generation/dissipation of species, s, by chemical reaction (kg/m^3-s)
t = time (sec)
T = temperature of gas mixture (K)
T_w = wall temperature (K)
V = mass average velocity of gas mixture (m/s)
Vol = fluid volume (m^3)
X_s = mole fraction of species, s
Y_s = mass fraction of species, s, in the bulk, and Y_s^w at the surface of the wall
W = molar weight of gas mixture (g/mol)
W_s = molar weight of species, s (g/mol)
W_c = molar weight of graphite (g/mol)
z = spatial coordinate
ε = convergence criterion
λ = thermal conductivity of gas mixture (W/m-K)
ρ = density of gas mixture (kg/m^3)
Ra = Rayleigh number
Re = Reynolds number
Nu = Nusselt number
Sc = Schmidt number
Sh = Sherwood number

References

1. J.O. Hirschfelder, C.F. Curtiss, and R.B. Bird, Molecular Theory of Gases and Liquids, 2nd Edition, Wiley (1964).

2. B.E. Poling, J.M. Prausnitz, and J.P. O'connell, The Properties of Gases and Liquids, 5th ed.,McGraw-Hill (2001).
3. K. Raznjevic, Handbook of Thermodynamic Tables and Charts, Hemisphere (1976).
4. J. B. Howard, G. C. Williams, and D.H. Fine, "Kinetics of carbon monoxide oxidation in postflame gases," 14th symposium (international) on combustion, 975 (1973).
5. H. Kawakami, "Air oxidation behavior of carbon and graphite materials for HTGR," TANSO, 124, 26 (1986).
6. M. Ogawa, "Mass transfer with graphite oxidation in gas mixture laminar flow through circular tube," J. At. Energy Soc. Jpn., 35(3), 245(1993).
7. M. Takahashi, M. Kotaka, and H. Sekimoto, "Burn-off and production of CO and CO_2 in the oxidation of nuclear reactor-grade graphites in a flow system," J. Nucl. Sci. Tech., 31(12), 1275 (1994).
8. E. L. Fuller and J. M. Okoh, "Kinetics mechanisms of the reaction of air with nuclear grade graphites: IG-110," J. Nuclear Materials, 240, 241 (1997).
9. T. Takeda and M. Hishida, "Studies on molecular diffusion and natural convection in a multi-component gas system," Int. J. Heat Mass Transfer, 39(3), 527 (1996).
10. M. Rossberg, Z. Elektrochem., 60, 952 (1956).
11. F.H. Harlow and A.A. Amsden, "A numerical fluid dynamics calculation method for all flow speeds," J. Comp. Phy., 8, 197 (1971).
12. M. Hishida and T. Takeda, "Study on air ingress during an early stage of a primary-pipe rupture accident of a high-temperature gas-cooled reactor", Nucl. Eng. Des., 126, 175 (1991).
13. FLUENT 6.0 User's Guide, FLUENT Inc. (2002).